

Efficiency of Super-Eddington Magnetically-Arrested Accretion

Jonathan C. McKinney^{1*}, Lixin Dai¹, Mark Avara²,

¹*University of Maryland at College Park, Dept. of Physics, Joint Space-Science Institute, 3114 Physical Sciences Complex, College Park, MD 20742, USA*

²*University of Maryland at College Park, Dept. of Astronomy, CSS 1231, College Park, MD 20742, USA*

Accepted 2015. Received 2015; in original form 2015.

ABSTRACT

The radiative efficiency of super-Eddington accreting black holes (BHs) is explored for magnetically-arrested disks (MADs), where magnetic flux builds-up to saturation near the BH. Our three-dimensional general relativistic radiation magnetohydrodynamic (GRRMHD) simulation of a spinning BH (spin $a/M = 0.8$) accreting at ~ 50 times Eddington shows a total efficiency $\sim 50\%$ when time-averaged and total efficiency $\gtrsim 100\%$ in moments. Magnetic compression by the magnetic flux near the rotating BH leads to a thin disk, whose radiation escapes via advection by a magnetized wind and via transport through a low-density channel created by a Blandford-Znajek (BZ) jet. The BZ efficiency is sub-optimal due to inertial loading of field lines by optically thick radiation, leading to BZ efficiency $\sim 40\%$ on the horizon and BZ efficiency $\sim 5\%$ by $r \sim 400r_g$ (gravitational radii) via absorption by the wind. Importantly, radiation escapes at $r \sim 400r_g$ with efficiency $\eta \approx 15\%$ (luminosity $L \sim 50L_{\text{Edd}}$), similar to $\eta \approx 12\%$ for a Novikov-Thorne thin disk and beyond $\eta \lesssim 1\%$ seen in prior GRMHD simulations or slim disk theory. Our simulations show how BH spin, magnetic field, and jet mass-loading affect the radiative and jet efficiencies of super-Eddington accretion.

Key words: accretion, black hole physics, (magnetohydrodynamics) MHD, radiation

1 INTRODUCTION

Black hole (BH) accretion drives a broad range of phenomena, including quasars, active galactic nuclei, BH X-ray binaries, some gamma-ray bursts, and tidal disruption events (TDEs). The disk’s gravitational potential energy and BH spin energy are converted into radiation, winds, and relativistic jets via magnetic stresses generated by the magneto-rotational instability (MRI) (Balbus & Hawley 1998), magnetic field threading the disk (Blandford & Payne 1982), or magnetic field threading the BH (Blandford & Znajek 1977). Magnetic torques are maximized when magnetic flux advects inward and piles-up until magnetic stresses balance incoming gas forces – the so-called magnetically-arrested disk (MAD) state (Narayan et al. 2003). Simulations of non-radiative MADs show up to $\sim 300\%$ total efficiency (Tchekhovskoy et al. 2011; McKinney et al. 2012), corresponding to 3 times the energy out as going into the BH. A fundamental question is: What form does this energy take at large distances and what fraction is radiative?

The radiative efficiency of BH systems is expected to be dependent upon the accretion rate \dot{M} , which controls the density, disk thickness, and dynamical importance of radiation (from gas-pressure dominated at low \dot{M} to radiation-pressure dominated at high \dot{M}). To scale $\dot{M}c^2$ or the radiative luminosity L , for a black hole mass M , speed of light c , gravitational constant G (giving

gravitational radius $r_g \equiv GM/c^2$), and Thomson electron scattering opacity κ_{es} , one can use the Eddington luminosity

$$L_{\text{Edd}} = \frac{4\pi GMc}{\kappa_{\text{es}}} \approx 1.3 \times 10^{46} \frac{M}{10^8 M_{\odot}} \text{ erg s}^{-1}. \quad (1)$$

One can also choose to normalize \dot{M} by $\dot{M}_{\text{Edd}} = (1/\eta_{\text{NT}})L_{\text{Edd}}/c^2$, where η_{NT} is the nominal accretion efficiency for the Novikov-Thorne thin disk solution (Novikov & Thorne 1973) (commonly, a fixed $\eta_{\text{NT}} = 0.1$ is used, but we include the spin dependence).

For luminosities $L \gtrsim 0.3L_{\text{Edd}}$, the accretion flow is expected to become geometrically thick and optically thick, and in this regime the photons can remain trapped within the flow as in the “slim disk” model (which includes no magnetic field) (Abramowicz et al. 1988). The super-Eddington accretion regime where $\dot{M} \gtrsim \dot{M}_{\text{Edd}}$ or $L \gtrsim L_{\text{Edd}}$ may help explain ultra-luminous X-ray sources as highly super-Eddington stellar-mass BHs (Watarai et al. 2001; Miller & Colbert 2004). Also, some black hole X-ray binaries can have $L \gtrsim L_{\text{Edd}}$ (e.g., SS433, Margon et al. 1979; Takeuchi et al. 2010; GRS1915+105, Fender & Belloni 2004), while tidal disruption events seem to require $\dot{M} \gg \dot{M}_{\text{Edd}}$ (Bloom et al. 2011).

In this paper, we seek to test whether super-Eddington MADs around spinning BHs are radiatively efficient. We use the general relativistic radiation magnetohydrodynamic (GRRMHD) code HARMRAD, which uses the M1 closure for radiation (McKinney et al. 2014). The slim disk model and recent radiative GRMHD simulations of non-MAD (i.e. lower magnetic flux than MAD on

* E-mail: jcm@umd.edu (JCM)

the BH and in the disk) super-Eddington flows are radiatively inefficient with $L \lesssim L_{\text{Edd}}$ even for $\dot{M} \sim 100\dot{M}_{\text{Edd}}$ (Sądowski et al. 2014; McKinney et al. 2014), far below the thin disk Novikov-Thorne (NT) efficiency (e.g. about 6% efficient for BH spin of $a/M = 0$ to 12% efficient for $a/M = 0.8$). However, MADs (not yet studied with radiation) can maximize the efficiency and may lead to a radiatively efficient state. This is also plausible for rapidly spinning BHs because MADs are then compressed into a thin disk (McKinney et al. 2012), which can lose radiation more rapidly.

We discuss the physical and numerical setup in §2. Results and discussions are presented in §3. We summarize in §4.

2 FULLY 3D GR RADIATIVE MHD MAD MODEL

This model with black hole mass of $M = 10M_{\odot}$ and dimensionless spin $a/M = 0.8$ has nominal thin disk efficiency $\eta_{\text{NT}} \approx 12.2\%$, so that $\dot{M}_{\text{Edd}} \approx 1.2 \times 10^{19} \text{ g/s}$ (see Eq. 1). While we choose a specific BH mass, the flow is strongly electron scattering dominated and so the results might apply roughly equally to all BH masses.

2.1 Opacities

We assume solar abundances (mass fractions of Hydrogen, Helium, and “metals”, respectively, $X = 0.7$, $Y = 0.28$, $Z = 0.02$) giving electron fraction $Y_e = (1 + X)/2$ and mean molecular weight $\bar{\mu} \approx 0.62$, entering gas entropy, pressure, and temperature T_g [Kelvin].

We use a frequency (ν) mean of the opacity α_{ν} to get an absorption-mean absorption opacity (units of $[\text{cm}^2/\text{g}]$) of $\kappa = (\int_{\nu} d\nu \alpha_{\nu} J_{\nu}) / (\int_{\nu} d\nu J_{\nu})$, where the absorbed radiation J_{ν} is assumed to be a Planck distribution at a radiation temperature of $T_r = (\hat{E}/a_{\text{rad}})^{1/4}$ [Kelvin], where $\hat{E} = u^{\mu} u^{\nu} R_{\mu\nu}$, u^{μ} is fluid 4-velocity, R is radiation stress-energy tensor, and a_{rad} is the radiation constant.

The electron scattering opacity is

$$\kappa_{\text{es}} \approx 0.2(1 + X)\kappa_{\text{kn}}, \quad (2)$$

where the Klein-Nishina correction for thermal electrons is $\kappa_{\text{kn}} \approx (1 + (T_g/(4.5 \times 10^8))^{0.86})^{-1}$ (Buchler & Yueh 1976).

The absorption-mean energy absorption opacity is

$$\kappa_{\text{abs}} \approx \left(\frac{1}{\kappa_{\text{m}} + \kappa_{H^-}} + \frac{1}{\kappa_{\text{Chianti}} + \kappa_{\text{bf}} + \kappa_{\text{ff}}} \right)^{-1}, \quad (3)$$

which bridges between different temperature regimes. The molecular opacity is $\kappa_{\text{m}} \approx 0.1Z$, and the H^- opacity is $\kappa_{H^-} \approx 1.1 \times 10^{-25} Z^{0.5} \rho^{0.5} T_g^{7.7}$. Rest-mass density, ρ , is in cgs units. The Chianti opacity accounts for bound-free at slightly lower temperatures and is given by $\kappa_{\text{Chianti}} \sim 4.0 \times 10^{34} \rho(Z/Z_{\text{solar}}) Y_e T_g^{-1.7} T_r^{-3.0}$ (this accounts for the assumed $Z = Z_{\text{solar}} = 0.02$ for figure 34.1 in Draine (2011), most applicable for baryon densities of $n_b \sim 1 \text{ cm}^{-3}$). The bound-free opacity is

$$\kappa_{\text{bf}} \approx 3 \times 10^{25} Z(1 + X + 0.75Y) \rho T_g^{-0.5} T_r^{-3.0} \ln(1 + 1.6(T_r/T_g)), \quad (4)$$

(Rybicki & Lightman 1986), where the $1 + X + 0.75Y$ term is roughly accurate near solar abundances, and the $\ln()$ term comes from fitting the absorption-mean integral. The free-free opacity is

$$\begin{aligned} \kappa_{\text{ff}} &\approx 4 \times 10^{22} (1 + X)(1 - Z) \rho T_g^{-0.5} T_r^{-3.0} \ln(1 + 1.6(T_r/T_g)) \\ &\times (1 + 4.4 \times 10^{-10} T_g), \end{aligned} \quad (5)$$

for thermal electrons and no pairs (see Eq. 5.25 in Rybicki & Lightman 1986 and Shu 1991). Thermal energy Comptonization is included as in Sądowski et al. (2015). The mean emission opacity

κ_{emit} is the same as κ_{abs} but letting $T_r \rightarrow T_g$, such that Kirchhoff's law gives an energy density emission rate of $\lambda = c\rho\kappa_{\text{emit}}a_{\text{rad}}T_g^4$. The total opacity is $\kappa_{\text{tot}} = \kappa_{\text{es}} + \kappa_{\text{abs}}$. The low-temperature opacities avoid unphysical opacity divergences during the simulation.

2.2 Initial Conditions

The initial disk is Keplerian with a rest-mass density that is Gaussian in angle with a height-to-radius ratio of $H/R \approx 0.2$ and radially follows a power-law of $\rho \propto r^{-0.6}$. The solution near and inside the inner-most stable circular orbit (ISCO) is not an equilibrium, so near the ISCO the solution is tapered to a smaller density ($\rho \rightarrow \rho(r/15)^7$, within $r = 15r_g$) and a smaller thickness ($H/R \rightarrow 0.2(r/10)^{0.5}$, within $r = 10r_g$ – based upon a low-resolution simulation). The total internal energy density u_{tot} is estimated from vertical equilibrium of $H/R \approx c_s/v_K$ for sound speed $c_s \approx \sqrt{\Gamma_{\text{tot}} P_{\text{tot}}/\rho}$ with $\Gamma_{\text{tot}} \approx 4/3$ and Keplerian speed $v_K \approx (r/r_g)/((r/r_g)^{3/2} + a/M)$. The total ideal pressure $P_{\text{tot}} = (\Gamma_{\text{tot}} - 1)u_{\text{tot}}$ is randomly perturbed by 10% to seed the MRI. The disk gas has $\Gamma_{\text{gas}} = 5/3$. The disk has an atmosphere with $\rho = 10^{-5}(r/r_g)^{-1.1}$ and gas internal energy density $e_{\text{gas}} = 10^{-6}(r/r_g)^{-5/2}$. The disk's radiation energy density and flux are set by local thermal equilibrium (LTE) and flux-limited diffusion (McKinney et al. 2014) with a negligible radiation atmosphere.

We do not use polish donuts (Abramowicz et al. 1978) or equilibrium tori as initial conditions. The outer parts of tori have an extended column of gas at high latitudes that contributes significantly to spurious luminosity (see section 6.8 in McKinney et al. 2014), trapping of the disk wind and radiation, and artificial (instead of the self-consistent wind) collimation of the jet.

The initial magnetic field is large-scale and poloidal. For $r < 300r_g$, the coordinate basis ϕ -component of the vector potential is

$$A_{\phi} = \text{MAX}(r^{\nu} 10^{40} - 0.02, 0)(\sin \theta)^{1+h}, \quad (6)$$

with $\nu = 1$ and $h = 4$. For $r \geq r_0 = 300r_g$, the field transitions to monopolar using $A_{\phi} = \text{MAX}(r_0^{\nu} 10^{40} - 0.02, 0)(\sin \theta)^{1+h(r_0/r)}$. The field is normalized with ~ 1 MRI wavelength per half-height H giving a ratio of average gas+radiation pressure to average magnetic pressure of $\beta \approx 24$ for $r < 100r_g$.

2.3 Numerical Grid and Density Floors

The numerical grid mapping equations and boundary conditions used here are identical to that given in McKinney et al. (2012). The radial grid of $N_r = 256$ cells spans from $R_{\text{in}} \approx 0.688r_{\text{H}}$ (horizon radius r_{H}) to $R_{\text{out}} = 10^5 r_g$ with cell size increasing exponentially till $r \sim 500r_g$ and then even faster. Radial boundaries use absorbing conditions. The θ -grid of $N_{\theta} = 128$ cells spans from 0 to π with mapping given in McKinney et al. (2012) but with $n_{\text{jet}} = 0.7$ to follow the jet, and other coefficients are slightly tuned so that the grid aspect ratio at $r \sim 30r_g$ is 1 : 2 : 3. Approaching the horizon (where the disk thins due to magnetic compression), the grid is tuned to follow the compressed disk, such that on the horizon there are 20 points across a half-height of the actual final disk with thickness of order $H/R \sim 0.1$. The Poynting-dominated polar jet contains, respectively, about 80, 60, 110 θ grid cells near the horizon, $r \sim 20r_g$, and $r \gtrsim 500r_g$. This gives sufficient resolution of the Poynting-dominated jet. The ϕ -grid of $N_{\phi} = 64$ cells spans uniformly from 0 to 2π with periodic boundary conditions.

As in our other papers (McKinney et al. 2012, 2013, 2014), we test the so-called convergence quality factors for the MRI in the θ and ϕ directions ($Q_{\theta, \text{MRI}}$ and $Q_{\phi, \text{MRI}}$) and turbulence ($Q_{\text{nlm, cor}}$) measuring, respectively, the number of grid cells per MRI wavelength

in the θ and ϕ directions and the number of grid cells per correlation length in the radial, θ and ϕ directions. At late times, our simulation has $Q_{\theta, \text{MRI}} \sim 340$, $Q_{\phi, \text{MRI}} \sim 45$, and rest-mass and magnetic energy densities have $Q_{\text{nlm}, \text{cor}} \sim 25, 20, 6$ at $r \sim 8r_g$, indicating good r, θ resolution and marginal ϕ resolution. We also measure the thickness of the disk per unit MRI wavelength, S_d , where $S_d < 0.5$ is where the MRI is suppressed. Initially $S_d \sim 0.6$ at all radii, while the time-averaged flow has $S_d \sim 0.1$ out to $r \sim 60r_g$.

The rest-mass and internal energy densities are driven to zero near the BH within the jet and near the axis, so we use numerical ceilings of $b^2/\rho = 300$, $b^2/e_{\text{gas}} = 10^9$, and $e_{\text{gas}}/\rho = 10^{10}$. The value of b^2/ρ is at the code's robustness limit for the chosen resolution.

2.4 Diagnostics

The disk's geometric half-angular thickness (H) per radius (R) is

$$\frac{H}{R}(r, \phi) \equiv \frac{H_0}{R} + \frac{\left(\int_{\theta} \rho(\theta - \theta_0)^n dA_{\theta\phi}\right)^{1/n}}{\left(\int_{\theta} \rho dA_{\theta\phi}\right)^{1/n}}, \quad (7)$$

with $n = 2$, $H_0/R = 0$, and surface differential $dA_{\theta\phi}$. One computes θ_0 like H/R , but let $n = 1$ and $\{\theta_0, H_0/R\} = \pi/2$.

The mass accretion rate and energy efficiency are, respectively,

$$\dot{M} = \left| \int \rho u^r dA_{\theta\phi} \right|, \quad (8)$$

$$\eta = -\frac{\int (T_t^r + \rho u^r + R_t^r) dA_{\theta\phi}}{[\dot{M}]_H}, \quad (9)$$

where T is the gas stress-energy tensor and $[\dot{M}]_H$ is the time-averaged \dot{M} on the horizon. The specific angular momentum accreted is $j = (\int (T_\phi^r + R_\phi^r) dA_{\theta\phi})/[\dot{M}]_H$. Both η and j are composed of free particle (PAKE=kinetic+gravitational), thermal (EN), electromagnetic (EM), and radiation (RAD) components. The jet is defined as PAKE+EN+EM, in locations where magnetic energy density exceeds rest-mass energy density. The wind is defined as PAKE+EN, located outside the jet. The wind can also contain untapped EM and RAD components. The dimensionless magnetic flux is

$$\Upsilon \approx 0.7 \frac{\int dA_{\theta\phi} 0.5|B^r|}{\sqrt{[\dot{M}]_H}}, \quad (10)$$

for field B in Heaviside-Lorentz units (McKinney et al. 2014).

To obtain the optical depth, at each instant in time we compute

$$\tau \approx \int \rho \kappa_{\text{tot}} dl. \quad (11)$$

For the radial direction, $dl = -f_r dr$, $f_r \approx u^r(1 - (v/c) \cos \theta)$, $(v/c) \approx 1 - 1/(u^t)^2$ (as valid at large radii), $\theta = 0$, and the integral is from $r_0 = 3000$ (being some radius beyond which only transient material would contribute to the optical depth, but a radius the disk wind has reached) to r to obtain $\tau_r(r)$. For the angular direction, $dl = f_r r d\theta$, $\theta = \pi/2$, and the integral is from each polar axis toward the equator to obtain $\tau_\theta(\theta)$. The flow's "true radiative photosphere" is defined as when $\tau_r = 1$, a conservative upper limit to the radius of the photosphere for an observer, because radiation can escape by tracking with relativistic low-density parts of the jet.

The radiative luminosity is computed at each instant as

$$L = - \int dA_{\theta\phi} R_t^r, \quad (12)$$

which is usually measured at $r = 400r_g$, where we only include those angles where the gas has $\tau_r(r) < 1$.

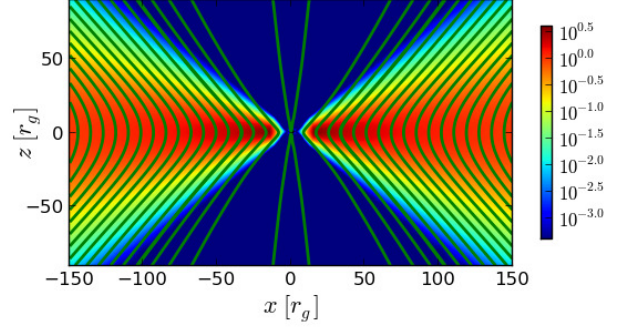


Figure 1. The initial ($t = 0$) state consists of a weakly magnetized radially-extended vertically-Gaussian disk with $H/R \sim 0.2$ around a spinning ($a/M = 0.8$) BH. Rest-mass density is shown as color with legend, while green lines show magnetic field lines. Density values are made dimensionless using \dot{M}_{Edd} , length r_g , and time r_g/c . The initial disk is threaded by weak (but ordered) magnetic flux, capable of accumulating onto the BH and leading to the MAD state.

3 RESULTS AND DISCUSSION

Fig. 1 and Fig. 2 show the initial and final state of the accretion flow. The initial disk is threaded by a weak large-scale poloidal magnetic field around a spinning black hole with $a/M = 0.8$. Rotation amplifies the magnetic field via the MRI leading to accretion of mass, energy, angular momentum, and magnetic flux. The magnetic flux accumulates and eventually forms a quasi-steady super-Eddington ($\dot{M} \sim 400L_{\text{Edd}}/c^2 \sim 50\dot{M}_{\text{Edd}}$) state that is a MAD (where the MRI is suppressed) out to $r \sim 60r_g$ after the model is evolved for a time $31, 200r_g/c$. The magnetically-compressed radiatively efficient thin disk near the BH is exposed by the jet channel, and the magnetized wind carries a significant fraction of radiation away from the disk.

Fig. 3 shows the mass accretion rate, efficiencies, disk thickness, and magnetic flux as time-averaged from $t = 30, 000r_g/c$ to $31, 200r_g/c$. The disk is in inflow and thermal equilibrium out to $r \sim 20r_g$ with constant fluxes of mass, energy, and specific angular momentum vs. radius. The total (kinetic + gravitational + electromagnetic + radiative) efficiency $\eta \approx 50\%$. As in non-radiative MAD models (Tchekhovskoy et al. 2011; McKinney et al. 2012), the efficiency is beyond the Novikov-Thorne value of $\eta_{\text{NT}} \approx 12\%$.

The magnetic field threading the BH is strong, with $\Upsilon \approx 10$ at late time and $\Upsilon \approx 8$ on average with $B_z \propto r^{-5/4}$ through the disk. The magnetic field threading the BH and disk leads to a magnetized wind that carries a significant amount of radiation away from the disk and helps to avoid the classical photon trapping effect of slim disks (Abramowicz et al. 1988). The magnetized wind at $r \sim 400r_g$ has a matter efficiency of about 15%, but the optically thick wind also contains about 15% trapped radiation energy and 10% electromagnetic energy that could be tapped for acceleration or heating. By $r \sim 400r_g$, the wind carries most of its radiation within a half-opening angle of 30° around the polar axes.

The Blandford-Znajek (BZ) effect leads to an electromagnetic, BZ, efficiency $\eta \sim 35\%$ on the BH. Some of that energy forms a jet with $\eta \sim 10\%$ at $r = 50r_g$, but some of that energy is absorbed by the wind, leading to a jet having only $\eta \sim 5\%$ by $r = 400r_g$.

Radiative-loading of magnetic field lines threading the BH leads to a lower-than-optimal BZ efficiency (relatedly, see Beskin et al. 2004; Takahashi & Ohsuga 2015) once the MAD state builds-up. The inertial loading of magnetic field lines is due to a total energy density $\rho_{\text{tot}} = \rho + e_{\text{gas}} + \hat{E}$ once $\tau \gtrsim 1$ caused by ρ keeping up with the MAD's higher b^2 when the numerical ceiling of

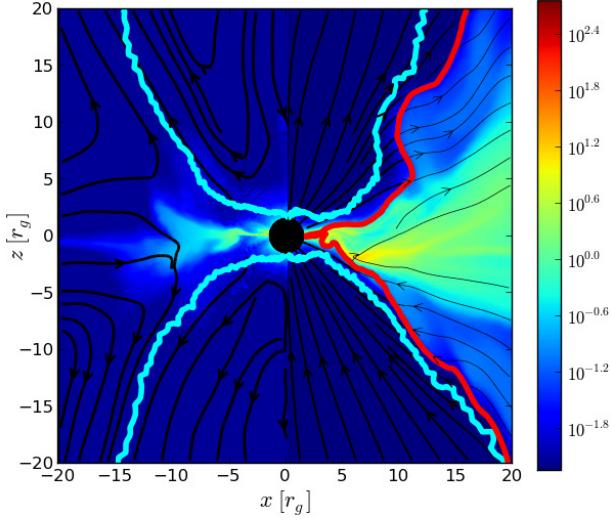


Figure 2. The evolved ($t = 31, 200r_g/c$) super-Eddington MAD state, with the figure split at $x = 0$ as two panels ($x < 0$ on left and $x > 0$ on right). Left panel shows radiation-frame radiation energy density (color, with legend), radiation velocity lines (black, fixed line width), and optical depth of unity away from each polar axis, $\tau_\theta = 1$ (cyan lines). Right panel shows fluid-frame rest-mass density (color, same legend), magnetic field lines (black, thicker lines for more magnetized gas), where magnetic energy is equal to rest-mass energy density (red lines), and same optical depth (cyan lines). The MAD state reaches a quasi-steady state out to $r \sim 20r_g$. Radiation advects inward within the equatorial disk, outward through the low-density jet channel, and outward along with the optically thick wind.

$b^2/\rho = 300$ is enforced. The optically thick radiation slows the jet magnetic field line rotation rate down by order unity compared to the optimal BZ value, because $b^2/\rho_{\text{tot}} \sim 1$ in the funnel (even if $b^2/\rho \gg 1$ there) as determined by the rough condition that the jet and disk have similar b^2 , yet $\Upsilon \gg 1$ implies that $b^2 \sim \rho$ in the disk, and radiative energy density $\hat{E} \sim \rho$ (from a thermal estimate of $H/R \sim c_s/v_K \sim 0.3$). A restarted simulation with an exponentially reduced (as b^2/ρ approached its ceiling) opacity has a BZ efficiency of $\eta \sim 100\%$ on the BH, as consistent with $\Upsilon \approx 8$ (Tchekhovskoy et al. 2011). A restarted simulation with a lower ceiling $b^2/\rho = 100$ led to a 20% BZ efficiency. So, mass-loading and opacity physics in the funnel are important to BZ-driven jets and winds for super-Eddington flows where radiation crosses magnetic field lines.

Fig. 4 shows the jet, wind, and “true” photosphere at large radii. The jet-wind boundary oscillates in angle to order unity, causing the wind to absorb some of the jet and radiation energy. We have resolved the true photosphere at $r \sim 400r_g$, and the radiation escaping to an observer has a high radiative efficiency of $\eta \approx 15\%$ (comparable with the NT value of $\eta \sim 12\%$), corresponding to luminosity $L \sim 50L_{\text{Edd}}$. Most of this radiation is within a half-opening angle of 15° around the polar axes. The luminosity in this GRRMHD MAD simulation is much higher than predicted by the slim disk solution at $\eta \sim 2\%$ or seen in other viscous non-MAD or non-MAD MHD simulations at $\eta \lesssim 1\%$ (Ohsuga et al. 2005; Ohsuga & Mineshige 2011; Sądowski et al. 2014; McKinney et al. 2014). Far beyond the photosphere, radiation might be absorbed (Sądowski & Narayan 2015) or some might leak out of the wind containing $\eta \approx 15\%$ in trapped radiation, but our grid is too unresolved to accurately track energy conversion for $r > 600r_g$. The radiation ultimately released is high in our simulation because 1) the disk near the BH is forced to become thin; 2) a magnetized wind pulls radiation-filled material off the disk; 3) the jet drills a channel and

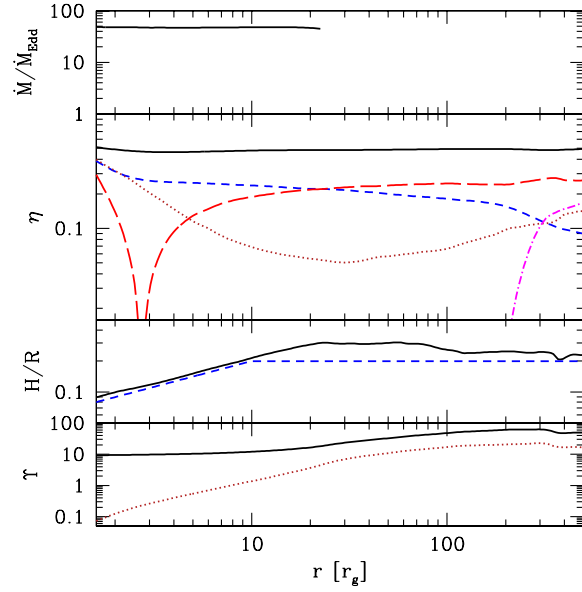


Figure 3. The time-averaged angle-integrated mass flux, efficiency, disk thickness, and magnetic flux. From top to bottom, panels are: Total mass accretion rate (\dot{M}) per unit \dot{M}_{Edd} out to where there is inflow and thermal equilibrium ($r \sim 20r_g$, beyond which the line is truncated), energy efficiency η (total: solid black line, electromagnetic: blue dashed, matter without rest-mass (i.e. kinetic+gravitational+thermal): dark red dotted, radiation (negative within $3r_g$): red long-dashed, radiative luminosity L : magenta dot-dashed), disk thickness H/R (evolved state: black solid, initial state: blue dashed), and magnetic flux (total on BH and threading disk: black solid, only threading disk: dark red dotted). The disk is magnetically compressed near the BH, and the thin disk generates a significant radiative flux that effectively releases starting at $r \sim 300r_g$. The initial disk with $H/R \approx 0.2$ has puffed up to $H/R \approx 0.3$ from $r \sim 20\text{--}70r_g$ after evolving for several thermal times. By $r \sim 400r_g$, the luminosity reaches $L \sim 50L_{\text{Edd}}$.

pushes back the opaque disk wind; and 4) the jet becomes conical at large radii allowing free-streaming of radiation. These lead to an effective diffusion timescale shorter than in the slim disk model.

We also performed otherwise identical simulations that are MAD with $a/M = 0$ as well as non-MAD simulations using a toroidal field in the initial disk (with $\beta \sim 20$ for all radii at the equator). The non-spinning MAD never produced a jet and the radiation remains trapped by the broad disk wind. Similarly, the toroidal field models with $a/M = 0$ and $a/M = 0.8$ show no low-density funnel region. Similar to Sądowski & Narayan (2015), our $a/M = 0$ MAD model with $\dot{M} \sim 20\dot{M}_{\text{Edd}}$ has a wind with NT-level efficiency of order 5% and negligible radiation flux at large radii by $r \sim 400r_g$ within the photosphere, because all radiation energy flux converted to kinetic energy flux. Our toroidal field models with $a/M = 0$ and $a/M = 0.8$ have $\dot{M} \sim \dot{M}_{\text{Edd}}$ with a wind efficiency of 2% and 4%, respectively, and a radiative efficiency of about 1%. So the formation of a low-density jet channel by a spinning BH, with enough magnetic flux to launch a jet and strong wind, helps super-Eddington accretion become radiatively efficient.

Convergence testing was performed by restarting each previously-mentioned model at a resolution twice lower in each dimension. The restarted simulation starts at half-way through the higher resolution simulation, and then the two resolutions are compared for the latter half of the simulations. We find that the total, BH, jet and radiative efficiencies, and Υ agree to within 30% or

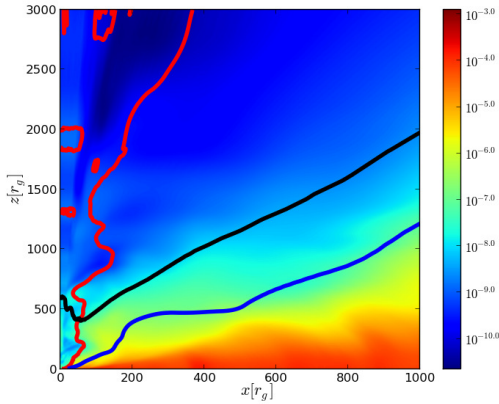


Figure 4. The evolved ($t = 31,200 r_g/c$) super-Eddington MAD state at large radii showing the jet, wind, and photosphere. Shows fluid-frame rest-mass density (color, with legend), where magnetic energy equal to rest-mass energy density (red lines), radiative photosphere at $\tau_r = 1$ (black line), and the wide-angle wind component's magnetic field line, within which (toward the polar axis) the outflow has achieved more than a single flow time along the line extending $\sim 1000 r_g$ (blue line). Quantities are ϕ -averaged. The jet extends to $r \sim 30,000 r_g$ with Lorentz factor $\gamma \sim 5$ by $r \sim 10^3 r_g$. The wind extends to $r \sim 3000 r_g$, with most of the wind's trapped radiation having an opening angle of 30° at $r \sim 400 r_g$. The disk at $R \gg 100 r_g$ has not evolved much. Radiation within $r \lesssim 400 r_g$ can more freely stream within the jet's low-density channel. By $t \sim 30,000 r_g/c$, at $r \sim 400 r_g$ within 15° around the polar axis, the outflow becomes conical and optically thin.

smaller error. Our convergence quality factors for the MRI and turbulence also suggest the simulations are converged.

A non-relativistic MHD simulation with $a/M = 0$ by Jiang et al. (2014) measured a NT-level radiative efficiency of about 5% that they attributed to MRI-driven magnetic buoyancy vertical transport of radiation. Their simulation had a small vertical extent $\pm 60 r_g$, so τ computed from Eq. 11 does not include the extended wind. Over extended distances, a significant portion of radiation energy flux can convert into wind energy flux (Sadowski & Narayan 2015). In our $a/M = 0.8$ MAD simulation, we attribute the high radiative efficiency to magnetic compression of the disk into a thin MAD, magnetized wind advection of radiation away from the disk, and the formation of a low-density jet channel through which radiation can more freely stream. Our simulation boundary is at $r \sim 10^5 r_g$, with accurate energy conversion out to $r \sim 600 r_g$. Our photosphere at $r \sim 400 r_g$ accounts for wind material that reached $r \gtrsim 3000 r_g$. If we ignore the extended wind, for the $a/M = 0.8$ MAD model we would miscalculate the radiative efficiency to be $\eta \sim 30\%$ – an overestimate by a factor of two. For the $a/M = 0$ MAD model, measuring at $r \sim 60 r_g$ gives $\eta \sim 5\%$ – an overestimate from $\eta \sim 0\%$ (caused the wind absorbing radiation energy).

4 SUMMARY

We have performed fully 3D simulations of super-Eddington accretion, including a simulation with $\dot{M} \sim 400 L_{\text{Edd}}/c^2 \sim 50 \dot{M}_{\text{Edd}}$ onto a rotating black hole with $a/M = 0.8$. Sufficient magnetic flux was distributed throughout the disk that the BH and disk reached MAD levels, where magnetic forces pushing out balance gas forces pushing in. The MAD state enabled the super-Eddington accretion flow to reach its maximum efficiency, with the total efficiency measured to be about 50% (higher for higher BH spins). Importantly,

the system has a high radiative efficiency of about 15% (luminosity $L \sim 50 L_{\text{Edd}}$) beyond the resolved photosphere at $r \sim 400 r_g$. This occurs because the magnetized wind carries radiation away from the disk. Also, the magnetized jet creates a low-density channel for radiation to more freely stream and pushes away the more opaque wind. These effects increase the radiative flux escaping the disk and diminish conversion of radiation energy flux into kinetic energy flux of the wind. This mechanism allows high radiative efficiencies from super-Eddington accretion systems.

As applied to jetted TDEs (Tchekhovskoy et al. 2014), our super-Eddington MAD simulations show how the jet and radiative efficiencies depend not only upon BH spin and magnetic flux but also upon jet mass-loading physics that leads to sub-optimal BZ efficiencies via dragging of BH field lines by optically thick radiation. Also, while the wind absorbs some jet energy, the jet channel exposes the (otherwise obscured) inner hot X-ray emitting disk.

ACKNOWLEDGMENTS

We thank Ramesh Narayan, Alexander Tchekhovskoy, Yan-Fei Jiang, and Aleksander Sadowski for discussions and acknowledge NASA/NSF/TCAN (NNX14AB46G), NSF/XSEDE/TACC (TG-PHY120005), and NASA/Pleiades (SMD-14-5451).

REFERENCES

- Abramowicz M., Jaroszynski M., Sikora M., 1978, *A&A*, 63, 221
- Abramowicz M. A., Czerny B., Lasota J. P., Szuszkiewicz E., 1988, *ApJ*, 332, 646
- Balbus S. A., Hawley J. F., 1998, *Reviews of Modern Physics*, 70, 1
- Beskin V. S., Zakamska N. L., Sol H., 2004, *MNRAS*, 347, 587
- Blandford R. D., Payne D. G., 1982, *MNRAS*, 199, 883
- Blandford R. D., Znajek R. L., 1977, *MNRAS*, 179, 433
- Bloom J. S., Giannios D., Metzger B. D., et al., 2011, *Science*, 333, 203
- Buchler J. R., Yueh W. R., 1976, *ApJ*, 210, 440
- Draine B. T., 2011, *Physics of the Interstellar and Intergalactic Medium*
- Fender R., Belloni T., 2004, *ARA&A*, 42, 317
- Jiang Y.-F., Stone J. M., Davis S. W., 2014, *ApJ*, 796, 106
- Margon B., Ford H. C., Katz J. I., et al., 1979, *ApJ*, 230, L41
- McKinney J. C., Tchekhovskoy A., Blandford R. D., 2012, *MNRAS*, 423, 3083
- McKinney J. C., Tchekhovskoy A., Blandford R. D., 2013, *Science*, 339, 49
- McKinney J. C., Tchekhovskoy A., Sadowski A., Narayan R., 2014, *MNRAS*, 441, 3177
- Miller M. C., Colbert E. J. M., 2004, *Int. J. Mod. Phys. and D13*, 1
- Narayan R., Igumenshchev I. V., Abramowicz M. A., 2003, *PASJ*, 55, L69
- Novikov I. D., Thorne K. S., 1973, in *Black Holes (Les Astres Occlus)*, edited by C. Dewitt, B. S. Dewitt, 343–450
- Ohsuga K., Mineshige S., 2011, *ApJ*, 736, 2
- Ohsuga K., Mori M., Nakamoto T., Mineshige S., 2005, *ApJ*, 628, 368
- Rybicki G. B., Lightman A. P., 1986, *Radiative Processes in Astrophysics*
- Sadowski A., Narayan R., 2015, *arxiv: 1503.00654*
- Sadowski A., Narayan R., McKinney J. C., Tchekhovskoy A., 2014, *MNRAS*, 439, 503
- Sadowski A., Narayan R., Tchekhovskoy A., Abarca D., Zhu Y., McKinney J. C., 2015, *MNRAS*, 447, 49
- Shu F. H., 1991, *The physics of astrophysics. Volume 1: Radiation*.
- Takahashi H. R., Ohsuga K., 2015, *PASJ*
- Takeuchi S., Ohsuga K., Mineshige S., 2010, *PASJ*, 62, L43
- Tchekhovskoy A., Metzger B. D., Giannios D., Kelley L. Z., 2014, *MNRAS*, 437, 2744
- Tchekhovskoy A., Narayan R., McKinney J. C., 2011, *MNRAS*, 418, L79
- Watarai K., Mizuno T., Mineshige S., 2001, *ApJ*, 549, L77-L77.